Int. J. Heat Mass Transfer. Vol. 36, No. 4, pp. 1097–1112, 1993
Printed in Great Britain

0017-9310/93 $6.00 + 0.00

Analysis of evaporation in the presence of composition/temperature gradient induced natural convection

SHOU-SHING HSIEH† and NAN-HUEI KUO
Department of Mechanical Engineering, National Sun Yat-Sen University, Kaohsiung, Taiwan 80424, R.O.C.

(*Received* 16 *July* 1991 *and in final form* 7 *January* 1992)

Abstract—A numerical analysis is performed to investigate the effects of the presence of combined composition and temperature gradient induced natural convection for evaporation from an open-topped tube which is partially filled with a liquid. Numerical solutions were carried out for water as the evaporation vapor and air as the gas. The present numerical results obtained at $Gr_T = 10^4$ and $Gr_L = 10^5$ with $Gr_M = 10^4$, 10^5 and 10^6, respectively, for a completely dry case (i.e. $\phi = 0$) and a relatively humid case (i.e. $\phi = 90\%$). Results were presented in terms of streamlines and isotherms as well as isohaline distributions. Numerical data show that there is no definite distribution among these three distributions as Gr_M is increased. However, the change seems to follow a definite trend and it is reasonable.

1. INTRODUCTION

THIS PAPER concerns the natural convection that is induced in a binary gas–vapor mixture due to evaporation at a liquid surface which bounds the mixture from below. Such a situation is complicated due to the simultaneous presence of differences in temperature and variations in concentration. The physical system to be considered here is an open-topped circular tube that is partially filled with a volatile liquid. The partial pressure of the vapor in the ambient is maintained at a lower value than that at the liquid surface, so that evaporation occurs. The temperature condition was chosen to simulate an oil storage tank exposed to the atmosphere ambient for the petroleum industry.

A survey of the literature revealed very few prior studies of natural convection either for simultaneous presence of differences in temperature and variations in concentration or for sole mass transfer problems. Sparrow *et al.* [1] carried out a numerical study for evaporation from an open-topped vertical tube which is partially filled with a liquid. Later, Nunez and Sparrow [2] presented an analytical model for isothermal and nonisothermal evaporation of a liquid from a partially filled cylindrical tube. Subsequent work reported by Sparrow and Nunez [3] was performed to provide a critical test of analytical/numerical models. In spite of this, only composition-induced natural convection was investigated. Aggarwal *et al.* [4] studied numerically buoyancy-driven flows of gases above liquids in a common enclosure with nonuniform heating from above. However, the paper only considered the differences in temperature.

In view of the foregoing discussion and an extensive review of the literature, it indicates that, indeed, no effort has been made to study evaporation in the simultaneous presence of composition and temperature-induced nature convection. It is believed that a substantial body or result is needed in order to have a complete description of heat transfer, mass transfer and flow fields in this important area of practical applications. For instance, the evaporation loss of an oil storage tank when it is exposed to the atmosphere.

Therefore, the main objective of this work is to investigate the effect of coupled thermal and mass diffusion on the velocity, temperature and concentration fields in the natural convection flow of a gas–liquid vapor mixture in a finite open-topped circular tube.

2. MATHEMATICAL FORMULATION

The system being studied is an open-topped vertical circular tube of finite length partially filled with liquid water (see Fig. 1 for details). The liquid surface and circumferential surfaces of the tube are maintained at a uniform temperature T_∞ higher than that of the bottom wall (T_0). This particular flow has obvious applications in the petroleum industry for the design and performance assessment of oil storage tanks. The moist air in the ambient is drawn into the tube by the simultaneous action of combined buoyancy forces due to temperature and concentration gradients. Since the molecular weight of water vapor is smaller than that of air, the buoyancy force due to mass transfer acts upwardly. As a result, in the present study the flow

†Author to whom correspondence should be addressed.

NOMENCLATURE

Ar aspect ratio, H/R
Ar_L aspect ratio for liquid phase, L/R
Ar_G aspect ratio for gas phase, h/R $(=Ar-Ar_L)$
B $(C_{p,1}-C_{p,2})(1-\omega_{1\infty})/C_p$
C_p specific heat [J kg^{-1} K^{-1}]
D mass diffusivity [m^2 s^{-1}]
F_b buoyancy per unit mass [m s^{-2}]
g acceleration due to gravity [m s^{-2}]
Gr_L Grashof number for liquid phase, $g\beta(T_\infty-T_0)R^3/\nu^2$
Gr_T Grashof number for heat transfer, $g(T_\infty-T_0)R^3/\nu^2T_\infty$
Gr_M Grashof number for mass transfer, $g(M_2/M_1-1)(1-\omega_{1\infty})R^3/\nu^2$
h distance between liquid surface and tube opening $(=H-L)$ [m]
h_{fg} latent heat of vaporization [J kg^{-1}]
H tube height [m]
k thermal conductivity [W m^{-1} K^{-1}]
L height of liquid pool [m]
M molecular weight [kg kmol^{-1}]
$\dot{m}$ evaporation rate [kg s^{-1}]
$\dot{m}''$ evaporation rate per unit area [kg m^{-2} s^{-1}]
p rescaled pressure $(p'+\rho_\infty gx)$ [kg m^{-1} s^{-1}]
p' pressure [kg m^{-1} s^{-1}]
P dimensionless pressure, $pR^2/\rho\nu^2$
Pr Prandtl number, ν/α
r radial coordinate [m]
R tube radius [m]
$\bar{R}$ universal gas constant [kg m^2 kmol^{-1} s^{-2} K^{-1}]
Re evaporation Reynolds number, $4\dot{m}/2\mu\pi R$
Sc Schmidt number, ν/D
T temperature [K]
u axial velocity [m s^{-1}]
U dimensionless axial velocity, uR/ν
v radial velocity [m s^{-1}]
V dimensionless radial velocity, vR/ν
W dimensionless mass fraction, $(\omega_1-\omega_{1\infty})/(1-\omega_{1\infty})$
x axial coordinate [m]
X dimensionless axial coordinate, x/R
X' dimensionless axial coordinate from interface, $X-Ar_L$.

Greek symbols
α thermal diffusivity [m^2 s^{-1}]
β thermal expansion coefficient [K^{-1}]
ζ dimensionless radial coordinate, r/R
θ dimensionless temperature, $(T_\infty-T)/(T_\infty-T_0)$
ν kinematic viscosity [m^2 s^{-1}]
ρ density [kg m^{-3}]
ϕ relative humidity
ω_1 mass fraction.

Subscripts
0 at initial condition or in the ground
1 component 1, vapor
2 component 2, air
∞ in the ambient
G gas phase
I in the interface
L liquid phase.

induced by the buoyancy force of mass transfer is retarded/counteracted due to $T_\infty > T_0$.

The governing equations for the present case are the incompressible steady Navier–Stokes equations along with conservation of component and energy for two-dimensional flow. The Boussinesq approximations (the concentration of water vapor in the mixture being very low and the temperature nonuniformity in the system being small) are employed to include the buoyancy effects due to temperature and concentration gradients. As stated earlier, the key feature of the analysis is the buoyancy term which appears in the x-momentum equation. At any point (x, r), the local body force F_b per unit mass can be written as:

$$\rho F_b = -\frac{\partial p'}{\partial x} - \rho g. \tag{1}$$

If $p = (p' + \rho_\infty gx)$, then equation (1) becomes

$$\rho F_b = -\frac{\partial p}{\partial x} - \rho g\left(1 - \frac{\rho_\infty}{\rho}\right) \tag{2}$$

in which ρ and ρ_∞ denote the densities of the mixture at point (x, r) and in the ambient at the open top of the tube, respectively.

2.1. *Governing equations*

2.1.1. *Liquid phase.* Using the Boussinesq approximation, ρ_∞ can be written as

$$\rho_\infty \approx \rho[1-\beta(T_\infty - T)]. \tag{3}$$

Therefore, the buoyancy force in the liquid phase can be represented as:

$$-\frac{\partial p}{\partial x} - \rho g\left(1 - \frac{\rho_\infty}{\rho}\right) = -\frac{\partial p}{\partial x} - \rho g\beta(T_\infty - T). \tag{4}$$

After introducing the following dimensionless variables,

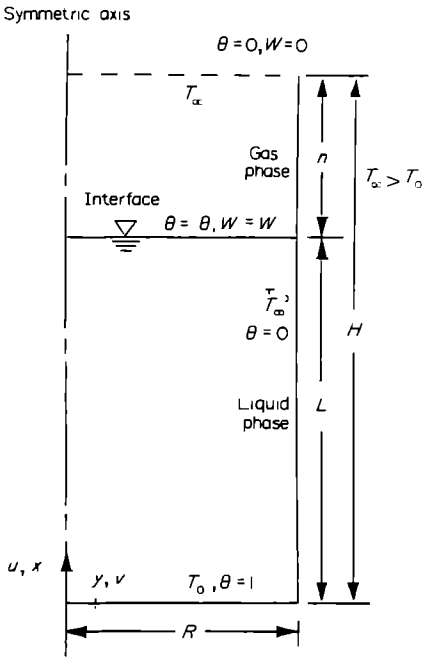

FIG. 1. Physical system of the present study.

$$X=\frac{x}{R},\quad \zeta=\frac{r}{R},\quad U=\frac{uR}{\nu},\quad V=\frac{\nu R}{\nu},\quad P=\frac{pR^2}{\rho\nu^2},$$

$$\theta=\frac{T_\infty-T}{T_\infty-T_0},\quad Pr_L=\frac{\nu}{\alpha}\ \text{and}\ Gr_L=\frac{g\beta(T_\infty-T_0)R^3}{\nu^2},$$

the liquid phase is governed by the following equations:

Continuity

$$\frac{\partial U}{\partial X}+\frac{1}{\zeta}\frac{\partial}{\partial\zeta}(\zeta V)=0 \tag{5}$$

X-Momentum

$$\frac{\partial}{\partial X}(UU)+\frac{1}{\zeta}\frac{\partial}{\partial\zeta}(\zeta VU)=-\frac{\partial P}{\partial X}+\frac{\partial^2 U}{\partial X^2}+\frac{1}{\zeta}\frac{\partial}{\partial\zeta}\left(\zeta\frac{\partial U}{\partial\zeta}\right)-Gr_L\,\theta \tag{6}$$

ζ-Momentum

$$\frac{\partial}{\partial X}(UV)+\frac{1}{\zeta}\frac{\partial}{\partial\zeta}(\zeta W)=-\frac{\partial P}{\partial\zeta}+\frac{\partial^2 V}{\partial X^2}+\frac{1}{\zeta}\frac{\partial}{\partial\zeta}\left(\zeta\frac{\partial V}{\partial\zeta}\right)-\frac{V}{\zeta^2} \tag{7}$$

Energy equation

$$\frac{\partial}{\partial X}(U\theta)+\frac{1}{\zeta}\frac{\partial}{\partial\zeta}(\zeta V\theta)=\frac{1}{Pr_L}\left[\frac{\partial^2\theta}{\partial X^2}+\frac{1}{\zeta}\frac{\partial}{\partial\zeta}\left(\zeta\frac{\partial\theta}{\partial\zeta}\right)\right]. \tag{8}$$

Equations (5)–(8) constitute a coupled nonlinear system for U, V, P and θ. The two prescribed parameters appearing in equations (6) and (8) are the Grashof number (Gr_L) and the Prandtl number (Pr_L).

2.1.2. *Gas phase.* The mixture can be treated as a perfect gas, so that

$$\rho=\frac{\rho M}{\bar{R}T},\quad \rho_\infty=\frac{\sigma_\infty M_\infty}{\bar{R}T}. \tag{9}$$

Since the variation of the pressure is very much smaller, this implies that the following approximation stands:

$$\left(1-\frac{\rho_\infty}{\rho}\right)\approx 1-\frac{T}{T_\infty}\frac{M_\infty}{M}. \tag{10}$$

Therefore,

$$\left(1-\frac{\rho_\infty}{\rho}\right)_c\approx\left(1-\frac{M_\infty}{M}\right)$$

and

$$\left(1-\frac{\rho_\infty}{\rho}\right)_t\approx\left(1-\frac{T}{T_\infty}\right).$$

Subscripts c and t denote the buoyancy due to concentration and temperature gradient alone, respectively.

It was assumed that the LHS of equation (10) could be decoupled:

$$\left(1-\frac{\rho_\infty}{\rho}\right)=\left[\left(1-\frac{\rho_\infty}{\rho}\right)_c+\left(1-\frac{\rho_\infty}{\rho}\right)_t\right].$$

The mixture's molecular weight can be expressed in terms of the molecular weights M_1 and M_2 of the components 1 and 2 (the vapor and the gas, respectively) and of their mass fractions ω_1 and ω_2:

$$1-\frac{M_\infty}{M}=1-\frac{\omega_1 M_2+(1-\omega_1)M_1}{\omega_{1\infty}M_2+(1-\omega_{1\infty})M_1}=\left(\frac{M_\infty}{M}-1\right)(\omega_{1\infty}-\omega_1). \tag{11}$$

The substitution of equation (11) into equation (2) with the above assumption yields

$$-\frac{\partial p}{\partial x}-\rho g\left(1-\frac{\rho_\infty}{\rho}\right)=-\frac{\partial p}{\partial x}-\rho g\left[\frac{T_\infty-T}{T_\infty}+\left(\frac{M_2}{M_1}-1\right)(\omega_{1\infty}-\omega_1)\right]. \tag{12}$$

Again, after introducing the following dimensionless variables,

$$X=\frac{x}{R},\quad \zeta=\frac{r}{R},\quad U=\frac{uR}{\nu},\quad V=\frac{\nu R}{\nu},\quad P=\frac{pR^2}{\rho\nu^2},$$

$$\theta = \frac{T_\infty - T}{T_\infty - T_0}, \quad W = \frac{\omega_1 - \omega_{1\infty}}{1-\omega_{1\infty}}, \quad Pr_G = \frac{\nu}{\alpha}, \quad Sc = \frac{\nu}{D},$$

$$Gr_T = \frac{g(T_\infty - T_0)R^3}{\nu^2 T_\infty},$$

$$Gr_M = \frac{g\left(\frac{M_2}{M_1} - 1\right)(1-\omega_{1\infty})R^3}{\nu^2}, \quad \text{and}$$

$$B = \frac{C_{p,1} - C_{p,2}}{C_p}(1-\omega_{1\infty}),$$

the governing equations for the gas phase can be written as:

Continuity

$$\frac{\partial U}{\partial X} + \frac{1}{\zeta}\frac{\partial}{\partial \zeta}(\zeta V) = 0 \tag{13}$$

X-Momentum

$$\frac{\partial}{\partial X}(UU) + \frac{1}{\zeta}\frac{\partial}{\partial \zeta}(\zeta VU) = -\frac{\partial P}{\partial X} + \frac{\partial^2 U}{\partial X^2} + \frac{1}{\zeta}\frac{\partial}{\partial \zeta}\left(\zeta \frac{\partial U}{\partial \zeta}\right) - Gr_T\,\theta + Gr_M\,W \tag{14}$$

ζ-Momentum

$$\frac{\partial}{\partial X}(UV) + \frac{1}{\zeta}\frac{\partial}{\partial \zeta}(\zeta W) = -\frac{\partial P}{\partial \xi} + \frac{\partial^2 V}{\partial X^2} + \frac{1}{\zeta}\frac{\partial}{\partial \zeta}\left(\zeta \frac{\partial V}{\partial \zeta}\right) - \frac{V}{\zeta^2} \tag{15}$$

Energy equation

$$\frac{\partial}{\partial X}(U\theta) + \frac{1}{\zeta}\frac{\partial}{\partial \zeta}(\zeta V\theta) = \frac{1}{Pr_G}\left[\frac{\partial^2 \theta}{\partial X^2} + \frac{1}{\zeta}\frac{\partial}{\partial \zeta}\left(\zeta \frac{\partial \theta}{\partial \zeta}\right)\right] + \frac{B}{Sc}\left(\frac{\partial \theta}{\partial X}\frac{\partial W}{\partial X} + \frac{\partial \theta}{\partial \zeta}\frac{\partial W}{\partial \zeta}\right) \tag{16}$$

Concentration equation

$$\frac{\partial}{\partial X}(UW) + \frac{1}{\zeta}\frac{\partial}{\partial \zeta}(\zeta VW) = \frac{1}{Sc}\left[\frac{\partial^2 W}{\partial X^2} + \frac{1}{\zeta}\frac{\partial}{\partial \zeta}\left(\zeta \frac{\partial W}{\partial \zeta}\right)\right]. \tag{17}$$

Equations (13)–(17) constitute another coupled nonlinear system for five variables U, V, P, θ and W. The four prescribed parameters are the Grashof numbers (Gr_T, Gr_M), the Prandtl number (Pr_G) and the Schmidt number (Sc).

2.2. *Boundary conditions*

2.2.1. *Liquid phase.* The boundary conditions are

$$X = 0, \quad U = 0, \quad V = 0, \quad \theta = 1 \tag{18}$$

$$\zeta = 0, \quad \frac{\partial U}{\partial \zeta} = 0, \quad V = 0, \quad \frac{\partial \theta}{\partial \zeta} = 0 \tag{19}$$

on the peripheral side

$$\zeta = 1, \quad U = 0, \quad V = 0, \quad \theta = 0. \tag{20}$$

2.2.2. *Gas phase.* The boundary conditions are

$$X = Ar, \quad \frac{\partial U}{\partial X} = 0, \quad V = 0, \quad \theta = 0, \quad W = 0 \tag{21}$$

$$\zeta = 0, \quad \frac{\partial U}{\partial \zeta} = 0, \quad V = 0, \quad \frac{\partial \theta}{\partial \zeta} = 0, \quad \frac{\partial W}{\partial \zeta} = 0 \tag{22}$$

on the peripheral side

$$\zeta = 1, \quad U = 0, \quad V = 0, \quad \theta = 0, \quad \frac{\partial W}{\partial \zeta} = 0. \tag{23}$$

Based on the extensive discussion reported in Sparrow *et al.* [1], a realistic boundary condition was employed as formulated in equation (21).

2.2.3. *Interface.* The surface of the liquid ($X = Ar_L$) was considered as being impermeable to the gas. In accordance with the impermeability condition, the naturally occurring diffusive flow of gas to the interface (diffusion from higher to lower concentration) must be balanced by a convective flow of gas away from the interface. This balance yields (at $X = Ar_L$ and any r)

$$\rho_2 u = \rho D \frac{\partial \omega_2}{\partial X}, \tag{24}$$

in which D is the mass diffusion coefficient. Since $\omega_2 = 1 - \omega_1$ and $\rho = \rho_1 + \rho_2$, equation (24), in dimensionless form, becomes

$$U_{G,I} = -\frac{1}{1-W_I}\frac{1}{Sc}\left(\frac{\partial W}{\partial X}\right)_{G,I} \tag{25}$$

where $W_I = (\omega_I - \omega_{1\infty})/(1-\omega_{1\infty})$. The interfacial mass fraction ω_I is obtained by assuming the gas–liquid interface to be in thermodynamic equilibrium; that is,

$$W_I = \frac{M_1 p_I}{M_2(p - p_I) + M_1 p_I} \tag{26}$$

where p_I stands for the corresponding saturation pressure at θ_I.

Equation (25) serves as the boundary condition for interface evaporation velocity. The boundary conditions for V at the interface can be derived from the shear force balance between the liquid and gas phases at the interface [5]; in dimensionless form, we have

$$\left(\frac{\partial V}{\partial X}\right)_G = \left(\frac{u_L}{u_G}\right)^2\left(\frac{\partial V}{\partial X}\right)_L. \tag{27}$$

For temperature boundary conditions, at $X = Ar_L$,

from the energy balance at the interface, the interfacial dimensionless temperature can be obtained as

$$-k_G\left(\frac{\partial\theta}{\partial X}\right)_G+\rho_G h_{fg}\frac{u_{G,I}}{(T_\infty-T_0)}=-k_L\left(\frac{\partial\theta}{\partial X}\right)_L. \quad (28)$$

In the present study, energy transport at the interface in the presence of mass transfer depends on two related factors. They are the gas temperature gradient at the interface and the rate of mass transfer.

3. NUMERICAL PROCEDURE

The governing differential equations (5)–(8), (13)–(17) and their boundary conditions were solved as an adaptation of an elliptic finite difference scheme (SIMPLEC) set forth in ref. [6]. Two computational domains are employed, the liquid and the gas phase are treated separately and the conditions (equations (27) and (28)) at the interface are used to match the velocity and temperature fields from both phases. The numerical methodology for treating the gas–liquid interface was exactly as in Prata and Sparrow [5]. Through Table 1, the grid dependence examination was made.

Finally, a 32×32 hybrid nonuniform/uniform grid was chosen. The layout of the grid in the liquid phase and the gas phase was arranged as follows:

(a) liquid phase

X-direction, $\Delta X_{max}=0.05Ar_L$ (nonuniform)
$\Delta X_{min}=0.0083Ar_L$ (nonuniform)

ζ-direction, $\Delta\zeta=0.05$ (uniform)

(b) gas phase

X-direction, $\Delta X_{max}=0.0489Ar_G$ (nonuniform)
$\Delta X_{min}=0.0083Ar_G$ (nonuniform)

ζ-direction, $\Delta\zeta=0.05$ (uniform).

A variable G is said to be convergent if its residual is smaller than a pre-assigned value. The residual is defined as

$$\beta=\max\left|\frac{G^n-G^{n-1}}{G^n}\right|_{i,j} \quad (29)$$

where n refers to the nth iteration and i, j stands for the node position. In the above expression, the residual β represents the maximum values throughout the computational region. The under relaxation values were 0.5 (for U), 0.6 (for V), 0.7 (for θ and W), and 0.8 (for P) respectively. The parameterization of the solutions will be presented and discussed. As stated earlier, the numerical solution was performed for water as the evaporating vapor and air as the gas. For this system, the Schmidt number Sc is 0.6 [7]. The reference condition is chosen at $T_\infty=37°C$, $T_0=23°C$, with an associated $Gr_L=10^5$ and $Gr_T=10^4$, $Gr_M=10^4$, 10^5 and 10^6, respectively, and a system pressure of 1 atm, while $\omega_I=0.04$ and $\omega_{I\infty}=0.0$ (completely dry ambient). For the second case, $\omega_I=0.04$ and $\omega_{I\infty}=0.036$ (ambient relative humidity of 90%) with the same corresponding values for Gr_M. The physical properties of the working medium (water/air) were chosen at $T=T_I+1/3(T_\infty-T_I)$ and $\omega=\omega_{I\infty}+1/3(\omega_I-\omega_{I\infty})$ [8] instead of the conventional average weighted values. The present numerical calculations were performed on a 486 IBM compatible PC.

4. RESULTS AND DISCUSSION

The results to be presented and discussed will begin with the rate of evaporation. Subsequently, to provide a basic understanding as well as to provide further insights, streamline, isothermal and isohaline maps, velocity and temperature profiles, and mass fraction profiles will be presented and discussed.

4.1. *Rate of evaporation*

The rate of evaporation at a differential area dA on the liquid surface ($x=L$) can be written as

$$\left[\rho_I u-\rho D\left(\frac{\partial\omega_I}{\partial x}\right)\right]dA \quad (30)$$

where both the convective and diffusive contributions have been included. By making use of equation (24) with $\partial\omega_2/\partial X=-\partial\omega_1/\partial X$ and noting that $\rho=\rho_1+\rho_2$, the expression in equation (30) becomes

$$\rho u\,dA \quad (31)$$

where $dA=2\pi r\,dr$. Therefore, the rate of evaporation can be expressed as:

$$\dot m=\int_0^R \rho u 2\pi r\,dr. \quad (32)$$

Table 1. Grid dependence examination for evaporation rate Reynolds number, absolute maximum stream function for liquid and gas flow, interface average temperature and bulk concentration

	17×7	22×12	27×17	32×22	37×27	42×32
Re	0.006121	0.006148	0.006154	0.006159	0.006156	0.006160
$\lvert\phi_L\rvert_{max}$	0.454384	0.649866	0.709724	0.737772	0.749904	0.737324
$\lvert\phi_G\rvert_{max}$	0.069731	0.052742	0.053888	0.058255	0.055292	0.058444
θ_I	0.001614	0.003758	0.003653	0.003585	0.003638	0.003565
W_b	0.001833	0.001843	0.001844	0.001845	0.001845	0.001846

The Reynolds number can be obtained in the following by incorporating $\dot{m}$ and the tube radius R for the tube flow:

$$Re = \frac{4\dot{m}}{2\pi R\mu} \tag{33}$$

$$Re = 4\int_0^1 U\zeta \, d\zeta. \tag{34}$$

Equation (34) was evaluated using the numerical integral scheme. As mentioned before, several grid sizes were tested and a comparison of the results among these computations is given in Table 1 for the evaporation rate Reynolds number, the absolute maximum stream function for liquid flow and gas flow, the interface average temperature and the bulk vapor concentration. It is noted that the differences in the evaporation Reynolds numbers, absolute maximum stream functions, interface temperatures and bulk mass fractions are less than 1%, by using 32×22 and 42×32 grids. Accordingly, the computation for the 32×22 grid is sufficient to understand the heat and mass characteristics in the flow. In addition to the grid dependence examination, the present numerical scheme was used to redevelop the case of Sparrow *et al.* [1] for both the completely dry ambient (i.e. $\omega_{1,\infty} = 0.0$) and very humid (i.e. $\omega_{1,\infty} = 0.036$) ambient conditions. The comparison shown in Fig. 2 reveals good agreement between both results. The numerical results for the evaporation rate are presented in Fig. 3, for $Ar_L = 2$, $Gr_L = 10^5$, $Gr_T = 10^4$, and $\omega_I = 0.04$ for two ambient conditions (one for the dry and one for the humid case) with $Gr_M = 10^4$ increased to $Gr_M = 10^6$. In this figure, the evaporation Reynolds number is plotted as a function of the gas–vapor space, which is in terms of Ar_G. Curves are included representing the present results for combined temperature and composition gradients and composition gradient alone, as well as those of the Stefan solution. Examination of the results of $Gr_L = 10^5$ and $Gr_T = 10^4$ for three different $Gr_M = 10^4$, 10^5, and 10^6 for the completely dry and humid cases, shown in Figs. 3(a) and (b), indicates that the Grashof number for mass transfer has a great influence on the evaporation rate. It is also seen, except for $Gr_M = 10^6$ and $\omega_{1,\infty} = 0.0$, that the evaporation rate decreases monotonically as the distance between the liquid surface and the tube opening increases. This behavior reflects the increased resistance to mass transfer associated with the greater transport length. On further examination of Fig. 3(a), at $Gr_M = 10^4$, it is seen that buoyancy evaporation rates, either due to a sole composition gradient or double diffusion, are nearly the same as those for the Stefan problem at the completely dry ambient. The result at $Gr_M = 10^5$ coincides with that given in Sparrow *et al.* [1], in which it was found that evaporation rates are 1–5 times those of the Stefan solutions. This is partly caused by the effect of the thermal and solutal buoyancies, which are comparable ($Gr_M = Gr_T = 10^4$), and partly by the counteracting effect of thermal buoyancy. As Gr_M is increased to 10^5, the discrepancy among these three solutions remains up to a distance between the liquid surface and the tube opening of 4.5. Among the discrepancy, double diffusion gives the highest evaporation rate to three times the Stefan value even though the thermal gradient reduces buoyancy. Concentration gradient induced buoyancy gives the values in between Stefan and double diffusion. At $Gr_M = 10^6$, this trend is quite different and the superiority is switched. However, composition gradient driven convection gives higher values than those

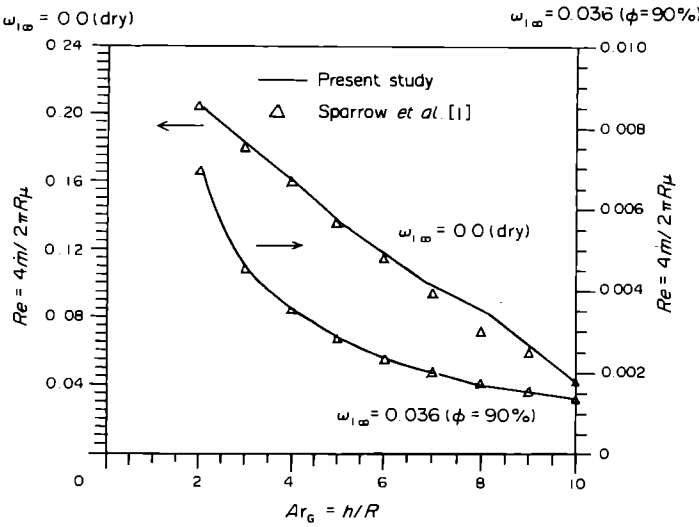

FIG. 2. Rerun Sparrow *et al.* [1] for $Gr_M = 10^4$, $\omega_I = 0.04$ (saturation), and for $\omega_{1,\infty} = 0.0$ ($\phi = 0\%$), $\omega_{1,\infty} = 0.036$ ($\phi = 90\%$).

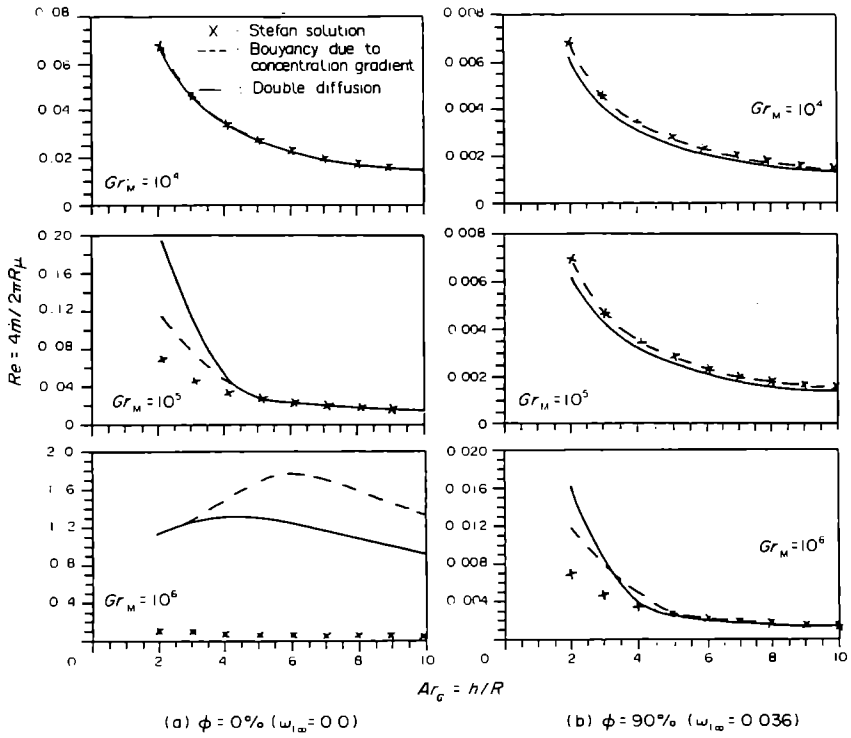

FIG. 3. Evaporation rates for $Ar_L = 2$, $Gr_L = 10^5$, $Gr_T = 10^4$, $\omega_I = 0.04$ (saturation) and: (a) $\omega_{I\infty} = 0.0$ ($\phi = 0\%$); (b) $\omega_{I\infty} = 0.036$ ($\phi = 90\%$).

of double diffusion. The enhancement stems from the dominance of the buoyancy-driven convection motions either by composition gradient alone or double diffusion, yielding evaporation rates up to 1.5–4.0 times the Stefan value. The peaks for composition gradient convection/double diffusion all happend at $Ar_G = 6$. The reason for this strange phenomenon still seems unclear at this stage. However, it is certain that the physical interaction due to mass and temperature gradients makes the problelm more complex than that discussed in Sparrow *et al.* [1].

The evaporation results in Fig. 3(b) convey a different message compared to Fig. 3(a). Here, the buoyancy evaporation rates for both thermal and solutal convection and solutal convection alone are, except for $Gr_M = 10^6$, the same as those for the Stefan problem. Following Sparrow *et al.* [1], the natural convection is unaffected in this case due to the small difference between the vapor mass fractions at the liquid surface and in the ambient (i.e. $\omega_I - \omega_{I\infty} = 0.004$), as is also reflected by the values of $Gr_M = 10^4$ and 10^5. However, the present study of double diffusion gives slightly lower values than those of the Stefan and sole composition gradient solutions as Ar_G increases. This is quite obvious because the present temperature gradients cause a counteracting effect in evaporation rates which results in an evaporation rate decrease. Moreover, at $Gr_M = 10^6$, a crossover point occurs at $Ar_G \approx 3$, where evaporation rates due to double diffusion are higher than those of the composition gradient alone when $Ar_G \geqslant 3$. Furthermore, it is found that, keeping the gas–vapor region fixed, the evaporation rate seems to be unchanged as the liquid space is varied (not shown here).

4.2. *Streamline distribution, isothermal map and isohaline distribution*

The streamline distribution information to be presented includes the results of the concentration gradient alone and double diffusion convection at two extreme ambient conditions. They are shown in Figs. 4 and 5, respectively. Moreover, to observe the gas–vapor space influences on the flow pattern, Fig. 6 is now added. Figure 4 shows three different Grashof numbers for mass transfer, $Gr_M = 10^4$, 10^5 and 10^6 for the dry and humid cases. Only the gas–vapor region is shown. For the completely dry ambient shown in Fig. 4(a), at $Gr_M = 10^4$, the streamline distribution indicates that the pattern of fluid flow is similar to a uniform upward flow. The evaporation vapor is represented by the streamlines which originated at the gas–liquid interface. As Gr_M is increased to 10^5, the presence of a U-shaped flow loop occurs. This indicates that the flow is downward in the outer annular and upward in the core, which is similar to that observed by Sparrow *et al.* [1]. Note that the downflowing fluid very nearly penetrates to the surface of

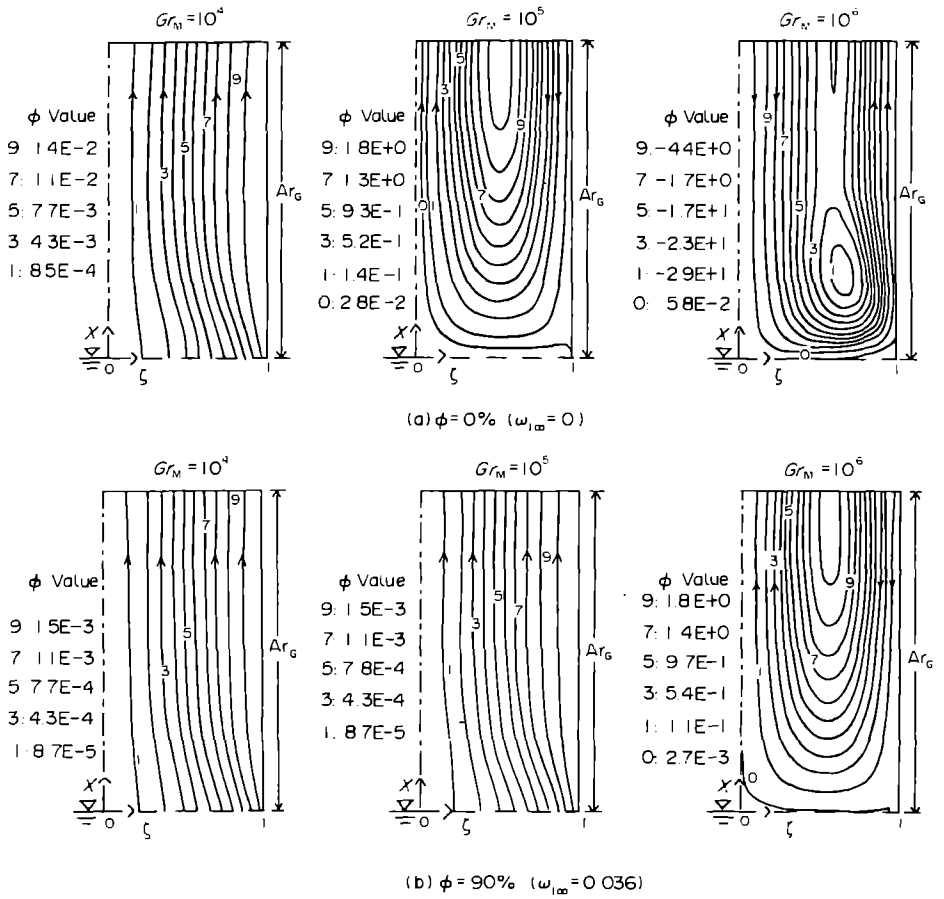

FIG. 4. Streamline distribution, concentration gradient only, for $Ar_G = 2$, $\omega_I = 0.04$ (saturation) and: (a) $\omega_{I\infty} = 0.0$ ($\phi = 0\%$); (b) $\omega_{I\infty} = 0.036$ ($\phi = 90\%$).

the liquid, whereupon it turns and sweeps across the surface as it moves radially inward. As can be seen in the figure, the circulating flow, upon approaching the tube axis, wells up from the liquid surface and streams upward to the tube opening. At $Gr_M = 10^6$, a small cell exists at the bottom of the gas–vapor region and, consequently, the U-shaped flow loop appears to be broken near the bottom of the gas phase. On the contrary, the flow is upward in the outer annulus and downward in the core. The strength of the streamline becomes stronger as Gr_M is increased. This can be seen for the absolute value of the streamline. On the other hand, for the humid case, shown in Fig. 4(b), the flow patterns are similar to those of the completely dry case, except for an occurrence delay for the U-shaped loop in the Gr_M effect. This is perhaps because the present temperature gradient counteracts the mass gradient and such an effect is significant in the humid case. Figure 5 shows the streamline maps for both gas–vapor and liquid regions for $Gr_M = 10^4$, 10^5, and 10^6, respectively, at the two ambient cases. Unlike composition gradient driven convection (see, for instance, Fig. 4 at $Gr_M = 10^5$), the flow from the U-shaped flow loop (see, for instance, Fig. 5 at $Gr_M = 10^5$) is swept in the outer annulus and downward in the core. After several trial runs, it is found that this phenomenon disappears when $Gr_L < 10^2$ and $Gr_T < 10$. The streamline map at $Gr_M = 10^4$ and 10^5 in gas–vapor region in Fig. 5(b) shows a dual cell recirculation. One thing worthy of mention here is that when the strength of streamline becomes weaker, in accordance with the shear force balance between liquid and gas flow at the interface, a recirculation cell is formed in the gas region adjacent to the interface (at $Gr_M = 10^4$ in Fig. 5(a), and $Gr_M = 10^4$ and 10^5 in Fig. 5(b)).

The above statements provide adequate reasons to explain why, for the humid case, the evaporation rates due to concentration gradient alone are a little higher than those of double diffusive convection, which may not always be the case as would be expected (see, for instance, Fig. 3(a) for $Gr_M = 10^5$ and Fig. 3(b) for $Gr_M = 10^6$). For the humid ambient case, in the liquid region, the streamline distribution displays dual recirculation cells for $Gr_M = 10^4$, 10^5 and 10^6. However, for the completely dry case, such behavior only occurs

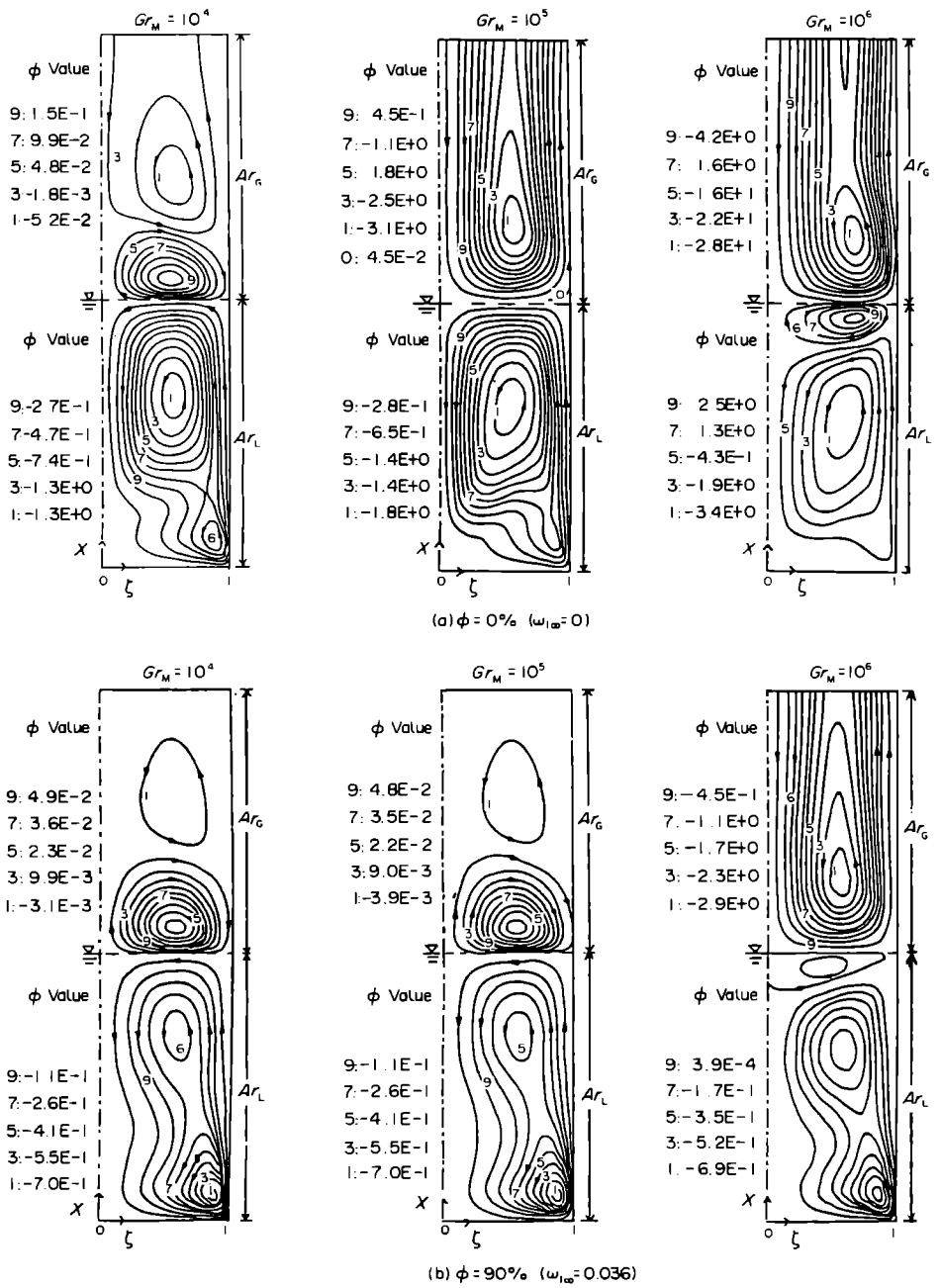

FIG. 5. Streamline distribution for $Ar_L = 2$, $Ar_G = 2$, $Gr_L = 10^5$, $Gr_T = 10^4$, $\omega_I = 0.04$ (saturation) and: (a) $\omega_{1,s} = 0.0$ ($\phi = 0\%$); (b) $\omega_{1,s} = 0.036$ ($\phi = 90\%$).

at $Gr_M = 10^4$. Since the liquid phase space does not affect the evaporation rate at all, as stated earlier, the present discrepancy will not be discussed. Further study may include this aspect. Figure 6 presents the effect of Ar_G (shortest/longest tube) on the flow pattern for the completely dry case. The flow pattern in the liquid phase seems to be independent of the variation of Ar_G. However, the flow patterns in the gas–vapor region do change slightly. This change confirms the previous finding that the tube opening increase reflects the increased resistance to mass transfer.

Figure 7 shows the isotherm contour maps corresponding to the flow discussed earlier in this section. Generally speaking, a low temperature distribution was found at the gas–vapor and liquid interface except at the bottom of the tube. For the liquid phase in Fig. 7(b), the thermal field is stratified fairly linearly in the vertical direction in most of the flow domain, especially in the liquid phase for a relatively humid case. In addition, for the humid case, it seems there is

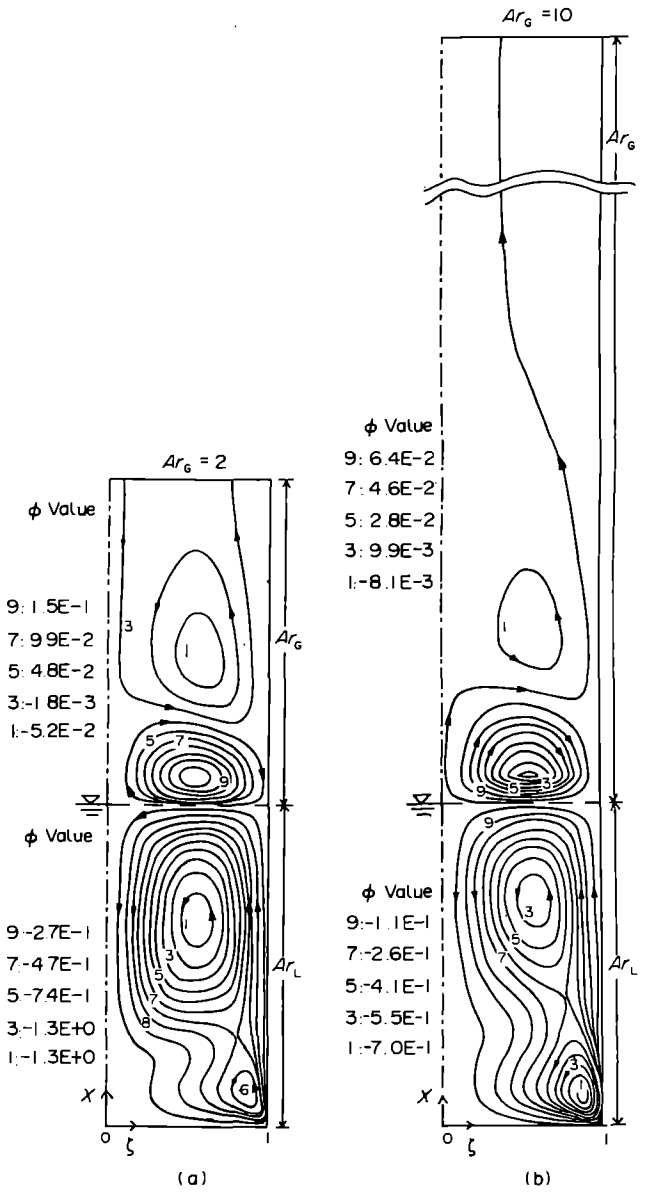

FIG. 6. Streamline distribution for $Ar_1 = 2$, $Gr_1 = 10^5$, $Gr_T = 10^4$, $Gr_M = 10^5$, $\omega_i = 0.04$ (saturation), $\omega_{i\infty} = 0.0$ ($\phi = 0\%$) and: (a) $Ar_G = 2$; (b) $Ar_G = 10$.

no interaction with the gas–vapor phase. However, it is important to note that radial temperature gradients exist. These radial temperature gradients, although small in magnitude, tend to be more pronounced in the regions closer to the tube wall. On the other hand, for the completely dry case, the temperature in the liquid phase does somehow interact with the gas–vapor temperature distribution. This phenomenon becomes more distinct as Gr_M is increased to 10^6. Further inspection of Fig. 7(a) reveals that the isothermal map pattern initially (at $Gr_M = 10^4$) behaves as stratified and later becomes a plume rise occupying almost the entire portion of the right half of the tube. This plume rise becomes more distinct and, consequently, results in the plume getting smaller as Gr_M is increased to 10^5. This can be seen by comparing the different plots in Fig. 7(a). This change somehow becomes moderate/delayed when compared to the corresponding plots for a relatively humid condition. The radial temperature gradients with plume rise phenomenon are essential to support the vertical velocity shear as evidenced by the corresponding streamline map, which results in convective heat transport evaporation due to the dominance of the evaporation in the main body of the flow field. Consequently, a narrow zone or annulus of intense vertical tem-

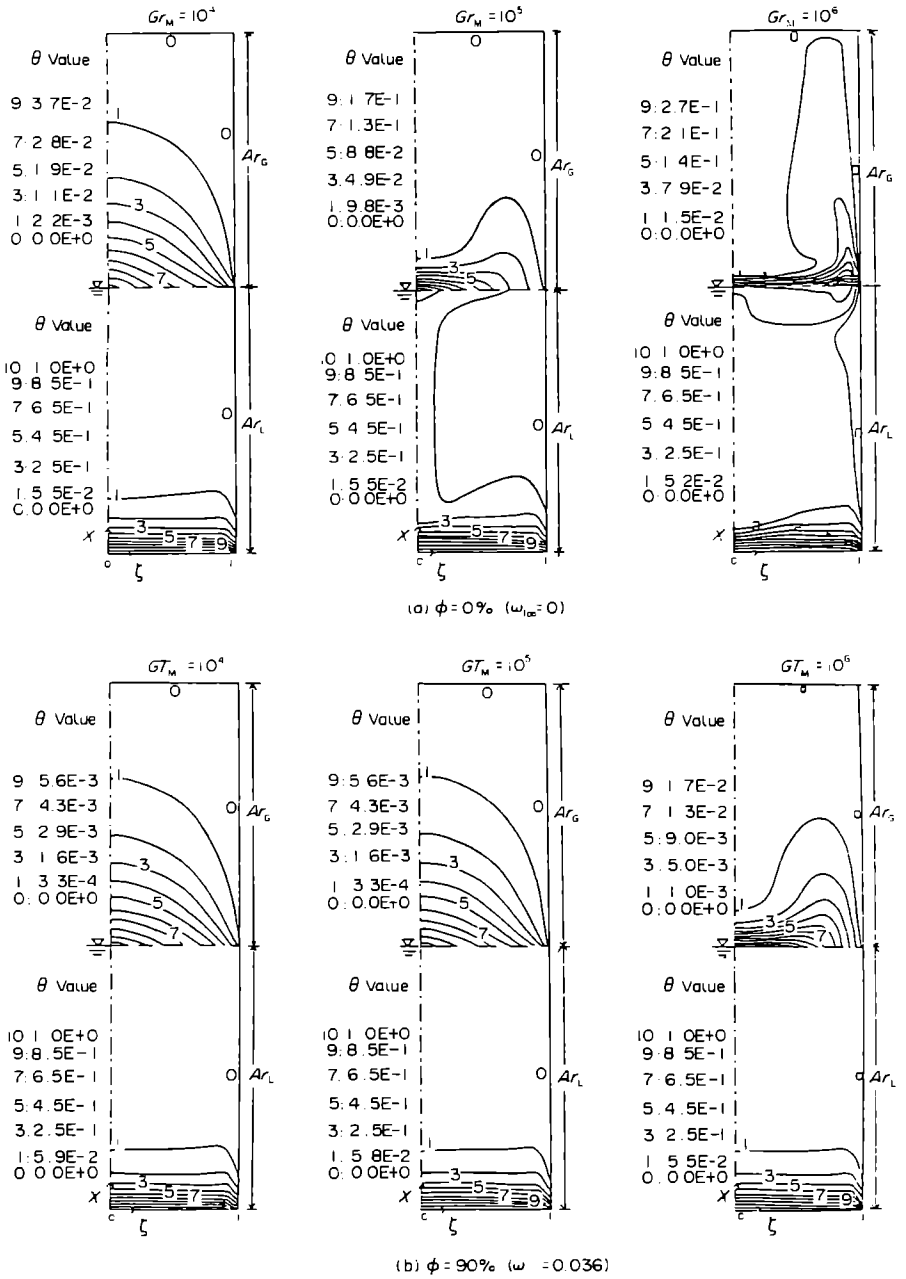

FIG. 7. Isothermal-line distribution for $Ar_L = 2$, $Ar_G = 2$, $Gr_L = 10^5$, $Gr_T = 10^4$, $\omega_1 = 0.04$ (saturation) and: (a) $\omega_{1\infty} = 0.0$ ($\phi = 0\%$); (b) $\omega_{1\infty} = 0.036$ ($\phi = 90\%$).

perature as well as radial gradients exist near the tube wall.

The isohaline distribution shown in Fig. 8 generally indicates that the concentration shows a near linear stratification in the vertical direction at $Gr_M = 10^4$. As Gr_M is increased further ($Gr_M = 10^5$, $\phi = 90\%$ and $Gr_M = 10^6$, $\phi = 90\%$), a radial concentration gradient exists.

At $Gr_M = 10^6$, the effect of solutal buoyancy outweighs the thermal effect, resulting in plume-like concentration distributions occupying a comparatively larger portion of the gas phase. Due to a high relative humidity for the case shown in Fig. 8(b) the concentration fields are still substantially linearly stratified in the vertical direction, even though Gr_M is increased to 10^5. Until $Gr_M = 10^6$, the layered structure vanishes, and the solutally driven flow comes into play in much of the gas phase.

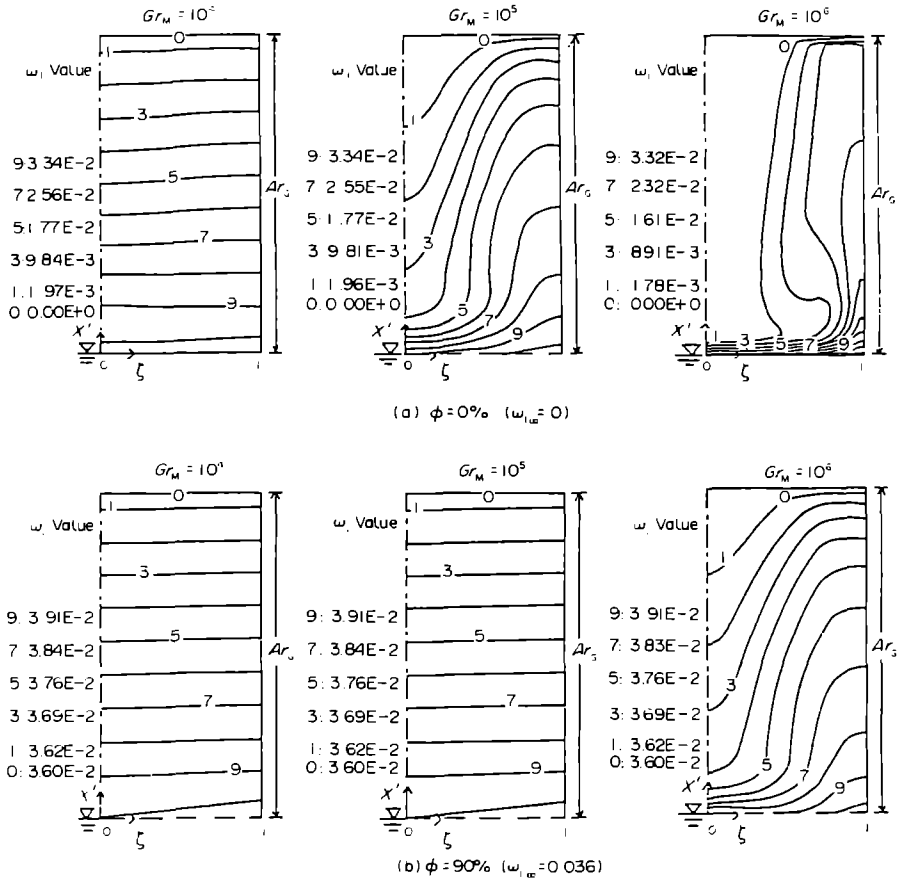

FIG. 8. Isohaline distribution for $Ar_L = 2$, $Ar_G = 2$, $Gr_L = 10^3$, $Gr_T = 10^4$, $\omega_1 = 0.04$ (saturation) and: (a) $\omega_{1,\infty} = 0.0$ ($\phi = 0\%$); (b) $\omega_{1,\infty} = 0.036$ ($\phi = 90\%$).

4.3. *Velocity profile, temperature distribution and mass fraction profile*

The evolution of the velocity fields and temperature distribution as well as mass fraction along the tube is respectively set forth in Figs. 9, 10 and 11 for the shortest of the investigated tube lengths, namely $Ar_G = 2$. Each figure displays a succession of velocity/temperature profiles and mass fractions parameterized by the dimensionless axial coordinate X'. On the ordinate, the velocity (temperature, concentration) is embedded in the dimensionless group uD/ν $((T_\infty - T)/(T_\infty - T_0), \omega_1)$ which can be regarded as a local Reynolds number (local temperature, local mass fraction). The most noteworthy feature of Fig. 9 is the two-lobed nature of the velocity profile. This shape is the same as that reported in Sparrow *et al.* [1]. In the central core of the tube, which extends from the centerline ($\zeta = 0$) to $\zeta \approx 0.6$, the U velocity is negative, indicating that flow is drawn into the liquid surface. This downward-directioned flow is drawn into the open top of the tube from the ambient. On the other hand, in the annulus which spans between the outer rim of the core and the tube wall, the flow is directed upward toward the open end of the tube as evidenced by the positive values of U. Generally speaking, it is interesting to note that the crossover from negative U to positive U occurs at virtually the same radial position at all axial elevations and, in addition, the crossover point is hardly affected by the gas–vapor space ratio Ar_G. Another significant feature of Fig. 9 is the magnitude of the velocities that are induced by natural convection. For both ambient cases, as Gr_M is increased, the velocity magnitudes (absolute values) increase. To provide a prospective for the velocity magnitudes displayed in these figures, it may be noted that the evaporation Reynolds number corresponding to the completely dry case is approximately 0.07 at $Gr_M = 10^4$ and $Ar_G = 2$. The evaporation Reynolds number can be written as $\bar{u}D/\nu$, where $\bar{u}$ is the mean velocity of the net downflow. In Fig. 9(a), the maximum downward velocity occurs at the center with the axial elevation at $X' = 0.28$ for $Gr_M = 10^4$ and is characterized by $uD/\nu \approx 2.5$, which is about 35 times larger than that ($uD/\nu \approx 0.07$) for the corresponding result of Fig. 4(a).

From the preceding discussion, it is clear that certain portions of the flow which streams upward through the annulus are evaporating vapor, while a

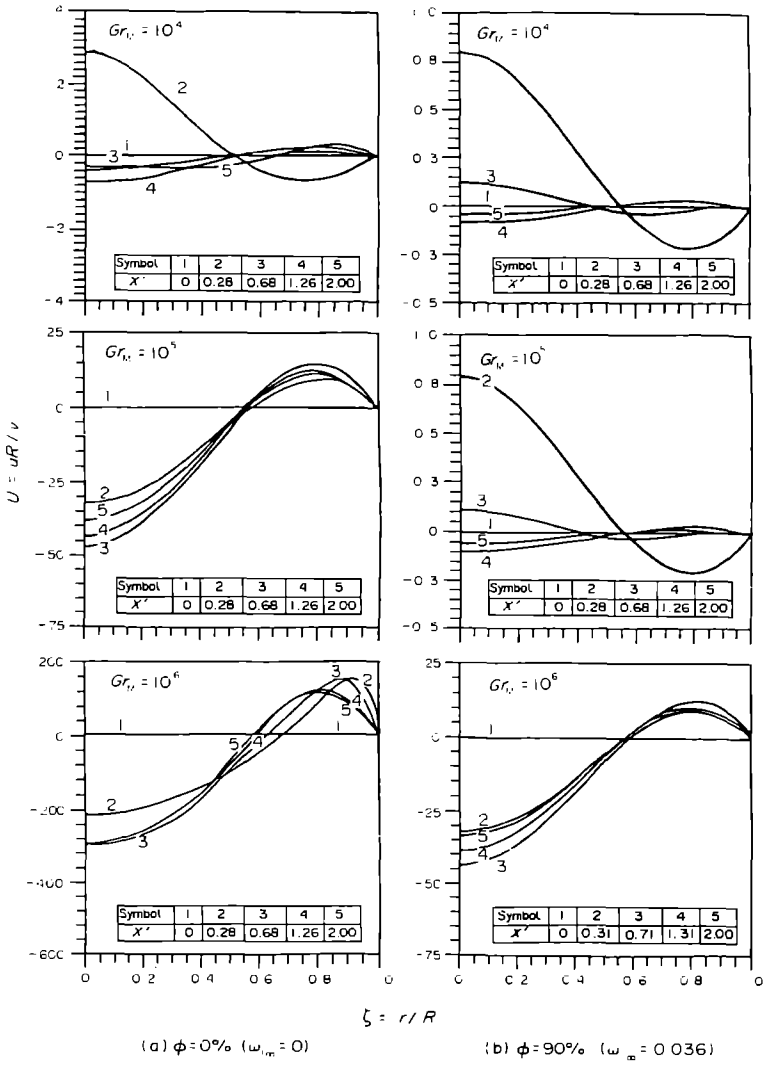

FIG. 9. Velocity profile for $Ar_L = 2$, $Ar_G = 2$, $Gr_L = 10^5$, $Gr_T = 10^4$, $\omega_I = 0.04$ (saturation) and: (a) $\omega_{1\infty} = 0.0$ ($\phi = 0\%$); (b) $\omega_{1\infty} = 0.036$ ($\phi = 90\%$).

certain portion of the annular flow consists of fluid that was drawn into the tube through the core. This indicates the presence of a U-shaped flow loop, with the downflow leg in the core and the upflow leg in the annulus.

On further inspection of Fig. 9, one can find that, for the completely dry case and $Gr_M = 10^4$, these studies indicate an evolution of the velocity profiles, which is virtually complete in the gas–vapor regions. This observation is witnessed by noting that there are gradual and steady changes between the profiles from $X' = 0$ to 0.28. This indicates that the maximum velocity (absolute value) occurs at $X' = 0.28$. However, for the remaining figures of Fig. 9, it is found that the maximum velocity occurs at the centerline of the tube and axial location at $X' = 0.68$, except for Fig. 9(b) at $Gr_M = 10^5$ ($X' = 0.28$) which is not the top of the tube. The reason for this is not clear at this stage.

Figure 10 represents the corresponding temperature distributions of Fig. 9. Generally speaking, the evolution of the temperature profile is virtually complete in the upper half of the gas–vapor region. As Gr_M is increased to 10^6, shown in Fig. 10(a), it is noteworthy that the temperature gradients near the vertical walls become steeper.

Profiles of the vapor mass fraction ω_1 are presented in Fig. 11. This figure is the counterpart of the velocity and temperature plots (Figs. 9 and 10). In the figure, curves are plotted at a succession of axial elevations. Based on the present boundary condition, one can find that the ω_1 profile at the tube opening ($X' = 2$) is horizontal and $\omega_{1\infty} = 0$ or 0.036 all across the opening, which is also confirmed by Sparrow *et al.* [1]. At any axial elevation, the vapor mass fraction increases from the tube axis to the wall. This trend is in accordance with the flow patterns illustrated in Fig. 5. The

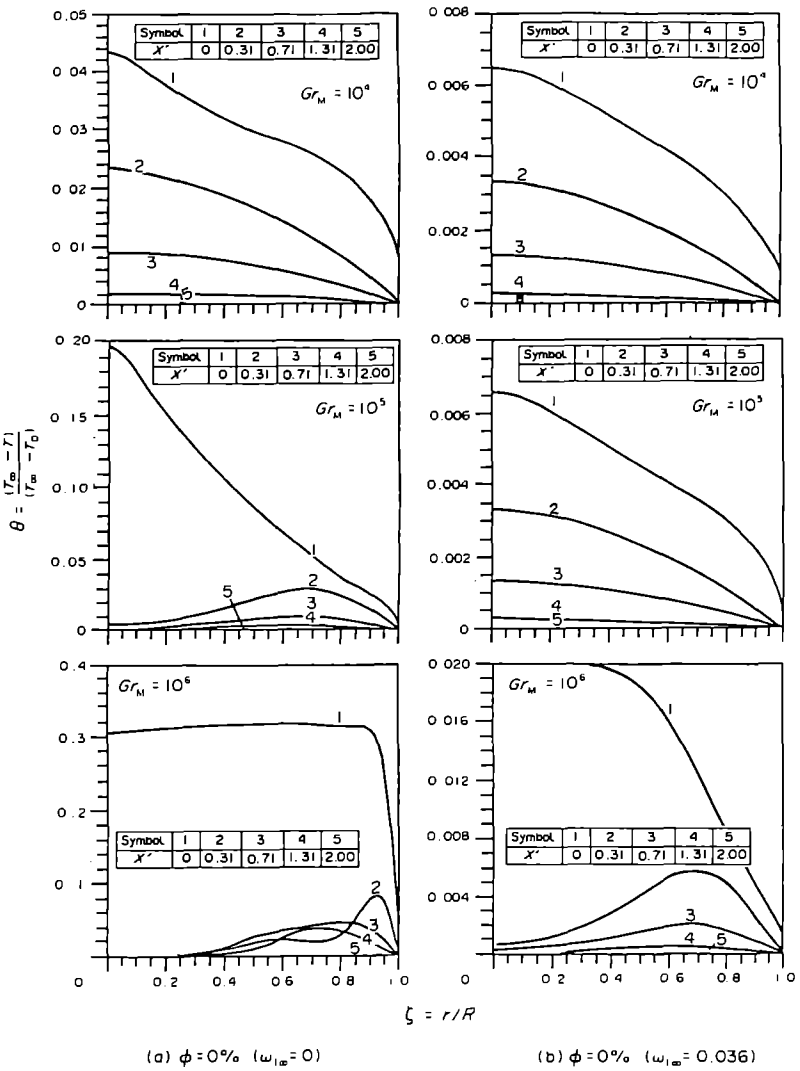

FIG. 10. Temperature profile for $Ar_L = 2$, $Ar_G = 2$, $Gr_L = 10^5$, $Gr_T = 10^4$, $\omega_l = 0.04$ (saturation) and: (a) $\omega_{l\infty} = 0.0$ ($\phi = 0\%$); (b) $\omega_{l\infty} = 0.036$ ($\phi = 90\%$).

extent of the radial variations is accentuated for the completely dry case, as can be verified by Fig. 11.

5. CONCLUSION

The nature of natural convection in the presence of composition/temperature gradients has been numerically studied for an open-topped tube which is partially filled with a liquid to broaden our basic understanding of this type of convective heat and mass transfer. The most significant contributions of the present study are the following.

(1) The present theoretical analysis of combined heat and mass transfer for an open-topped tube which is partially filled with water has made it possible to examine for the first time the effect of a number of parameters. For instance, Gr_M, Gr_T, Gr_L and Ar_G for two extreme ambient conditions ($\phi = 0$ and 90%).

(2) The streamline distribution indicates that a U-shaped flow loop most likely occurs at $Gr_M \geqslant 10^5$. The upflow leg of the loop is formed in the core of the tube and the downflow leg is formed in the annular region adjacant to the tube wall. At $Gr_M = 10^4$, this loop does not exist, and two toroidal recirculation zones occur instead.

(3) Isotherms corresponding to the flow field in remark (2) show that the thermal field is stratified fairly linearly in the vertical direction in most of the flow domain, especially in the liquid phase. Radial temperature gradients are found to exist and, although small in magnitude, they tend to be more pronounced in the regions closer to the tube wall.

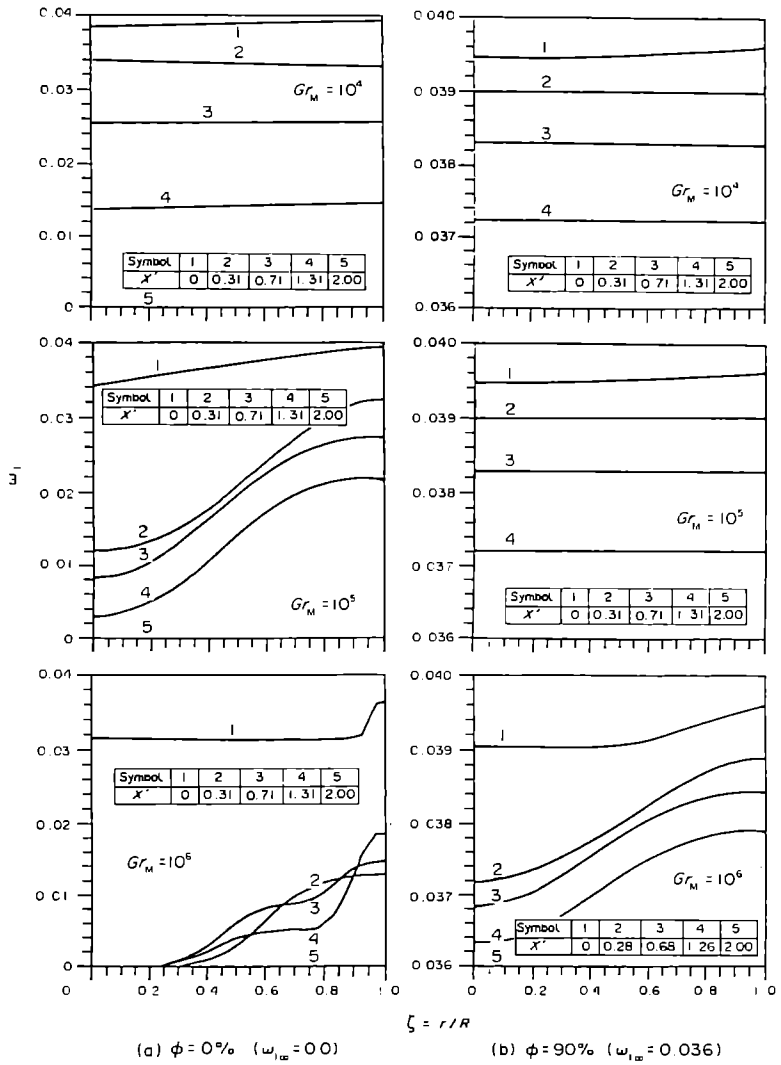

FIG. 11. Profile of the vapor mass fraction for $Ar_L = 2$, $Ar_G = 2$, $Gr_L = 10^5$, $Gr_T = 10^4$, $\omega_I = 0.04$ (saturation) and: (a) $\omega_{I\infty} = 0.0$ ($\phi = 0\%$); (b) $\omega_{I\infty} = 0.036$ ($\phi = 90\%$).

Moreover, there is an interaction with the gas–vapor phase for the liquid phase at $Gr_M = 10^5$ and a plume rise occurs in the gas–vapor phase. This is essential to support the vertical velocity shear as evidenced by the corresponding streamline map, which results in convective heat transport evaporation.

(4) The isohaline distribution indicates that the concentration shows a near linear stratification in the vertical direction at $Gr_M = 10^4$. As Gr_M is increased to 10^5, a radial concentration gradient exists. The temperature field is qualitatively akin to the solutal domain convection and the overall velocity in the bulk of the tube is fairly upward near the tube wall.

(5) The aspect ratio Ar_G seems to have no significant influence on the velocity field as well as the temperature and concentration distribution at a definite Grashof number (Gr_T, Gr_L, Gr_M), which is essential to support the vertical velocity shear. This explanation shows that convective heat transport is dominant for evaporation.

(6) The evaporation rate decreases as the gas–vapor region aspect ratio increases for $Gr_M \leqslant 10^5$, as confirmed by Sparrow *et al.* [1]. Furthermore, the temperature gradient seems to have certain different influences on the evaporation rates at different ambient conditions.

(7) The effect of the variations of Grashof number for mass transfer Gr_M is not clearly noted. From Figs. 4 and 5, it is not easy to obtain a definite trend to describe the influence as Gr_M is varied at a fixed Gr_L and Gr_T.

Acknowledgements—The authors are grateful to the referee who provided detailed and constructive comments. This work was supported in part by a research grant from China Petroleum Refinery Company (Taiwan, R.O.C.).

REFERENCES

1. E. M. Sparrow, G. A. Nunez and A. T. Prata, Analysis of evaporation in the presence of composition-induced natural convection, *Int. J. Heat Mass Transfer* **28**, 1451–1460 (1985).
2. G. A. Nunez and E. M. Sparrow, Model and solutions for isothermal and nonisothermal evaporation from a partially filled tube, *Int. J. Heat Mass Transfer* **33**, 461–477 (1988).
3. E. M. Sparrow and G. A. Nunez, Experiments on isothermal and nonisothermal evaporation from partially filled, open-topped vertical tubes, *Int. J. Heat Mass Transfer* **33**, 1345–1355 (1988).
4. S. K. Aggarwal, J. Iyengar and W. A. Sirignano, Enclosed gas and liquid with nonuniform heating from above, *Int. J. Heat Mass Transfer* **29**, 1593–1604 (1986).
5. A. T. Prata and E. M. Sparrow, Evaporation mass and heat transfer from a lid-driven cavity, *Numer. Heat Transfer* **13**, 27–48 (1988).
6. J. P. Van Doormaal and G. D. Raithby, Enhancements of the SIMPLE method for predicting incompressible fluid flows, *Numer. Heat Transfer* **7**, 147–163 (1984).
7. R. C. Reid, J. M. Prausnitz and T. K. Sherwood, *The Properties of Gases and Liquids*. McGraw-Hill, New York (1966).
8. L. C. Chow and J. N. Chung, Evaporation of water into a laminar steam of air and superheated steam, *Int. J. Heat Mass Transfer* **26**, 147–163 (1983).